Journal of Applied Physics

Mechanisms of titania nanoparticle mediated growth of turbostratic carbon nanotubes and nanofibers

Cite as: J. Appl. Phys. **122**, 014301 (2017); https://doi.org/10.1063/1.4990291
Submitted: 30 March 2017 . Accepted: 14 June 2017 . Published Online: 06 July 2017

A. Kudo, S. A. Steiner, B. C. Bayer, P. R. Kidambi, S. Hofmann, M. S. Strano, and B. L. Wardle

Mechanisms of titania nanoparticle mediated growth of turbostratic carbon nanotubes and nanofibers

A. Kudo,[1,a)] S. A. Steiner III,[2] B. C. Bayer,[3,b)] P. R. Kidambi,[3,c)] S. Hofmann,[3] M. S. Strano,[4] and B. L. Wardle[2,d)]
[1]*Department of Materials Science and Engineering, Massachusetts Institute of Technology, 77 Massachusetts Ave., Cambridge, Massachusetts 02139, USA*
[2]*Department of Aeronautics and Astronautics, Massachusetts Institute of Technology, 77 Massachusetts Ave., Cambridge, Massachusetts 02139, USA*
[3]*Department of Engineering, Electrical Engineering Division, University of Cambridge, 9, JJ Thomson Avenue, Cambridge CB3 0FA, United Kingdom*
[4]*Department of Chemical Engineering, Massachusetts Institute of Technology, 77 Massachusetts Ave., Cambridge, Massachusetts 02139, USA*

(Received 30 March 2017; accepted 14 June 2017; published online 6 July 2017)

Turbostratic carbon nanotubes (CNTs) and nanofibers (CNFs) are synthesized by chemical vapor deposition using titania nanoparticle catalysts, and a quantitative lift-off model is developed to explain CNT and CNF growth. Micron-scale long turbostratic CNTs and CNFs were observed when acetylene is utilized as a carbon feedstock, and an alumina substrate was incorporated to improve the homogeneity of catalyst distribution. Turbostratic CNTs/CNFs are always found attached to nanoparticle corners, in the absence of the graphitic cage that is typically observed with metal nanoparticle-mediated growth. The observed morphology in turbostratic CNTs/CNFs supports a model in which several layers of graphene lift off from high-curvature corners of the titania nanoparticle catalysts. This model explains a key feature, which differentiates the growth of turbostratic CNTs/CNFs via non-metallic nanoparticles from growth using standard metal nanoparticle catalysts. The observed CNT/CNF growth and the accompanying model can impact the assessment of other metal-oxide nanoparticle catalysts, with the findings here contributing to a metal-free synthesis of turbostratic CNTs/CNFs. *Published by AIP Publishing.* [http://dx.doi.org/10.1063/1.4990291]

I. INTRODUCTION

Carbon nanostructures including carbon nanotubes (CNTs) and nanofibers (CNFs) are attractive for a wealth of applications from high-strength composite materials[1] and carbon-based electronics,[2,3] to energy devices.[4,5] CNT/CNF synthesis by chemical vapor deposition (CVD) often uses metal nanoparticle catalysts,[6–8] but recent studies have pointed out that the metal nanoparticle catalysts can be detrimental for several prospective applications. For example, they may react with substrate in an unwanted manner during CVD and hence constrain the choice of substrate materials,[9] or the metal residue within the obtained carbon nanostructures would be toxic to human bodies.[10] Non-metallic nanoparticles, especially those that are not reduced to a metal at commonly used CVD temperatures (700 °C to 1000 °C), have therefore been recently investigated as alternative catalysts. Metal oxides, such as zirconia,[11] titania,[12] tantala,[13] and alumina,[14] constitute the principal class of non-metallic nanoparticle catalysts for both CNTs and CNFs. Some of those species,[15] along with magnesia[16] and hafnia[17] nanoparticles, also serve to synthesize few-layer graphenes. Group 14 elements including their compounds, such as nanoparticles of silicon carbide, silicon, germanium,[18] silica,[19] and diamond,[20] are reported to show catalytic activity to grow CNTs.

In order to acquire insights into the growth mechanism mediated by those non-metallic nanoparticles, high-resolution transmission electron microscopy (HRTEM) is a highly desired characterization tool. We previously identified two different types of carbon nanofibrils grown from zirconia nanoparticle catalysts by HRTEM.[21] Zirconia nanoparticles in those growths did not have graphitic cages that are observed with conventional metal nanoparticle catalysts, suggesting a surface bound growth mechanism that does not involve solution of carbon atoms in the nanoparticle catalysts.[22,23]

While the number of species reported as active non-metallic catalysts is increasing, the combinations of CVD parameters have not been investigated broadly. For example, although silica and titania as catalysts are more frequently reported than other non-metallic species, silica nanoparticle catalysts are mostly evaluated with methane as carbon feedstock,[19,24–26] and titania nanoparticles with ethanol as carbon feedstock,[12,27,28] with some cases that switch these feedstock between silica and titania.[26,29–31] This is a conspicuous difference from research on metal nanoparticle catalysts, which has reported a variety of combinations of catalysts and carbon feedstock.[32–35] The extant studies on metallic

[a)]Current address: Department of Applied Physics and Materials Science, California Institute of Technology, 1200 E California Blvd., Pasadena, CA 91125, USA.
[b)]Current address: Faculty of Physics, University of Vienna, Boltzmanngasse 5, A-1090 Vienna, Austria.
[c)]Current address: Department of Mechanical Engineering, Massachusetts Institute of Technology, 77 Massachusetts Ave., Cambridge, MA 02139, USA.
[d)]wardle@mit.edu.

nanoparticle catalysis have shown a spectrum of results, which has enabled researchers evaluate the key parameters for reproducible high-yield production of CNTs and understand the growth mechanisms.[8,36,37] Therefore, similar studies on non-metallic nanoparticle catalysts are required to optimize catalysis towards higher yield.

Here we show titania nanoparticle-mediated CVD syntheses of turbostratic carbon nanofibrils. Acetylene and ethylene are converted into few microns-long turbostratic CNTs and CNFs. The growth yield is enhanced by the combination of several parameters including the nature of the carbon feedstock, the CVD temperature, time, and the chemistry of the substrate. The highest growth yield is obtained using acetylene at 850 °C for 30 min on alumina-sputtered substrates. We contextualize our results by quantitative estimations for lift-off of carbon nanofibril growth, where graphitic layers with a certain thickness form over a metal-oxide nanoparticle corner and lift off due to strain energy build-up in the bent graphene layers, thereby initiating a repetitive mechanism for forming turbostratic carbon nanofibrils. This model supports the HRTEM characterization of CNTs/CNFs obtained from acetylene and ethylene carbon feedstock. Our results can guide further exploration of controllable metal-free synthesis of CNTs and CNFs.

II. METHODS

A. Catalyst precursor solution

Precursor solution was prepared with isopropanol (IPA, VWR, CAS No 67-63-0, >99.5%) and titanium oxysulfate hydrate procured from Sigma-Aldrich (TiOSO 4· xH_2O CAS 13825-74-6). 0.16 g of the titanium oxysulfate hydrate was dissolved in 15.72 g (20 ml) of IPA to make saturated solution. After ultrasonicating for 3 min and leaving the solution to settle for a day, sediment and saturated supernatant were separated. The supernatant was used as the catalyst precursor throughout the experiments in this work.

B. Sample preparation

Two types of substrates were prepared: silicon wafer with thermally grown 200 nm thick silica layer (called silica substrate in this article) and with 13 nm of alumina further on top of the silica layer (called alumina substrate in this article). A stoichiometric alumina target (99.995%) was sputtered on to the silica substrate by an RF magnetron sputtering machine (CCR) using argon gas (99.9995%) at 2.5×10^{-4} mbar to prepare alumina substrate. The prepared supernatant catalyst solution was dropcast on these substrates so that appropriate amount of nanoparticle catalyst was deposited. Two different substrates presented different catalyst morphologies due to different wetting behavior with IPA. On alumina substrate, the nanoparticle catalysts were more homogeneously distributed than on silica substrate and so was CNT/CNF growth. After the IPA evaporates completely, the samples were pyrolyzed under a flow of 200 sccm of argon at 800 °C for 3 to 4 h.

C. CVD process and characterization

The five growth process conditions implemented in this work are summarized in Table I. The carbon feedstock employed in the process is indicated as follows: A for acetylene, E for ethylene, and M for methane. Recipes with each carbon feedstock species are based on our previous experience growing CNTs using metal and zirconia nanoparticles.[11,13,38,39]

Recipes A and M use a 2 in. diameter tube furnace with the outer diameter $\phi = 51$ mm and the length L = 400 mm, whereas recipe E uses a 1 in. tube furnace with the outer diameter $\phi = 25$ mm and the length L = 360 mm. For recipe A, the temperature was ramped to the set point at a rate of ~20 °C/min under a 1000 sccm argon flow, followed by an additional 4000 sccm argon flow for 5 min. A flow of 500 sccm hydrogen and 200 sccm argon was then introduced for 3 min, and then CVD started. After CVD, 4000 sccm argon flow was added for 5 min and then the system cooled down. For recipe M, the temperature was ramped to the set point at a rate of ~20 °C/min under a flow of 1000 sccm argon, and then 200 sccm of hydrogen was introduced for 10 min before CVD started. After CVD, a 4000 sccm argon flow was added for 5 min and then the system cooled down. For recipe E, after 2 min of flushing tube with 750 sccm of argon, the temperature is ramped to the set point at a rate of ~50 °C/min under a flow of 100 sccm argon and 400 sccm hydrogen. Then CVD started, and after the reaction the system started to cool down. For the parameters used in each CVD, see Table I. All CVD processes were done under atmospheric pressure. Prepared samples were imaged by SEM (Zeiss Sigma-VP and Zeiss Ultra 55) and transferred onto TEM grids by scraping for HRTEM characterization (JEOL 2010F). Samples prepared by recipe A-3 are investigated by Raman spectroscopy (Horiba Jobin Yvon MR800, 532 nm laser) and XPS (Thermo Scientific K-Alpha XPS system).

Two different reaction temperatures, 750 °C and 850 °C, were chosen to compare the effect on growth in the typically employed range of temperatures for high growth yield without excessive pyrolytic soot formation in gas phase. The most homogeneous and highest growth yield was observed in recipe A-3. HRTEM images and fast Fourier transformation

TABLE I. Summary of CVD recipes implemented in this work.

Recipe	Feedstock	Temperature (°C)	Time (min)	Gas (sccm)	Substrate
A-1	Acetylene	750	30	$Ar:C_2H_2:H_2 = 200:10:500$	Silica
A-2	Acetylene	750	30	$Ar:C_2H_2:H_2 = 200:10:500$	Alumina
A-3	Acetylene	850	30	$Ar:C_2H_2:H_2 = 200:10:500$	Alumina
E	Ethylene	750	15	$Ar:C_2H_4:H_2 = 100:100:400$	Silica
M	Methane	900	15	$CH_4:H_2 = 500:100$	Alumina

(FFT) patterns were used to determine species and phase of the nanoparticle catalyst. Sample labels delineate different conditions within the same carbon feedstock. All CVD recipes were implemented with a control sample, a substrate which had no catalyst precursor on it in order to ensure no inherent contamination was present, especially metals, that could grow carbon nanostructures. Recipes A-1, A-2, A-3, and M were also performed with a baseline metal-growth sample comprised of alumina-sputtered silicon with Fe nanoparticle catalysts. In this work, none of all the control samples showed neither growth nor changes in morphology (see supplementary material, Sec. I), and baseline samples with Fe nanoparticle catalysts always grew CNTs for all of the listed recipes, as expected.

III. RESULTS AND DISCUSSION

First, carbon nanostructures were synthesized with acetylene (A-1, A-2, and A-3). Recipe A-1 shows 1–3 μm long carbon nanofibrils, with some occasionally grown longer than 5 μm, as shown in Fig. 1(a). In recipe A-1 with a silica substrate, we observe a circular residue from evaporation of catalyst precursor solvent, causing inhomogeneous catalyst deposition and resulting in the growth of carbon nanofibrils exclusively within these regions. Recipe A-2 improves the homogeneity of catalyst distribution by using an alumina substrate, presumably due to more favorable solvent wetting and de-wetting to form a more uniform alumina nanoparticle precursor film. By raising the reaction temperature to 850 °C from recipe A-2, recipe A-3 yields homogeneous and relatively high growth yield of carbon nanofibrils about 1–3 μm long as annotated [Figs. 1(b) and 1(c)]. We investigate the most homogeneous growth (A-3) in more detail using HRTEM. Crowds of turbostratic carbon nanofibrils, few tens to some hundreds nanometers long, are observed. The growth is a mixture of CNTs (Fig. 2) and CNFs (Fig. 3). Their diameters are ~12 nm according to sampling from multiple TEM micrographs, similar to the nanoparticle diameter of ~10 nm. The HRTEM images suggest that CNTs/CNFs are formed via a base growth and attached to only the corners of the nanoparticles and their agglomerates, without forming graphitic cages encapsulating the nanoparticle catalysts often observed with metal nanoparticles.[6,7] This morphology is similar to the growth mechanism occurring on the catalyst surface observed with unreduced zirconia nanoparticles[21] and hence infers a mechanism different from one that involves solution and precipitation of carbon atoms[40,41] and/or that the structures of the substrate surface affect the resulting growth by the interaction through the encapsulating graphitic cage.[42,43] A substructure is observed within CNTs where few graphitic layers form a bundle, as indicated in Figs. 2(b) and 2(e).

The point-localized energy dispersive X-ray spectroscopy (EDX) shown in Fig. 2(c) is one method used to eliminate the concern of growth originating from metal catalyst contaminants (Fe and Cr are common) rather than from titania studied herein. No peaks from these contaminants are observed. In order to further exclude contamination and assign the phase for the nanoparticle imaged by HRTEM, a table of lattice distances and corresponding Miller indices is created for Fe (α and γ phases),[44,45] iron carbide (Fe_3C),[46] Cr,[47] Ti (α and β phases),[48,49] titania (anatase, rutile, and brookite),[50] and titanium carbide (for approximately $0.2 \leq x \leq 1$ of TiC_x),[51] which is available in the supplementary material, Sec. II (see Table S1, supplementary material).

XPS spectra of carbon (C1s), oxygen (O1s), and titanium (Ti2p) taken before and after CVD with recipe A-3 are shown in Fig. 4. While C1s peaks present mostly adventitious carbon contamination, the major peak at 285 eV slightly shifts toward lower binding energy after CVD, indicating the formation of sp^2 carbon: namely CNTs and CNFs.[52] No C1s peaks typical of titanium carbide are seen around 282 eV.[53] O1s peaks are primarily observed from the sputtered alumina layer (531.4 eV) and native oxide over the silicon wafer (532.5 eV).[54] The moderate decrease in intensity around 530 eV after CVD may be attributed to partial depletion of oxygen from titania,[55] which is observed around 1000 °C with solid carbon[56,57] or by hydrogen around 450 °C.[58,59] Ti2p peaks before and after CVD show Ti^{4+} at 458.9 eV (Ref. 60) from titania and do not indicate Ti in titanium metal[61] and carbide[60] around 454–455 eV, implying that the growth is primarily obtained from titania. These

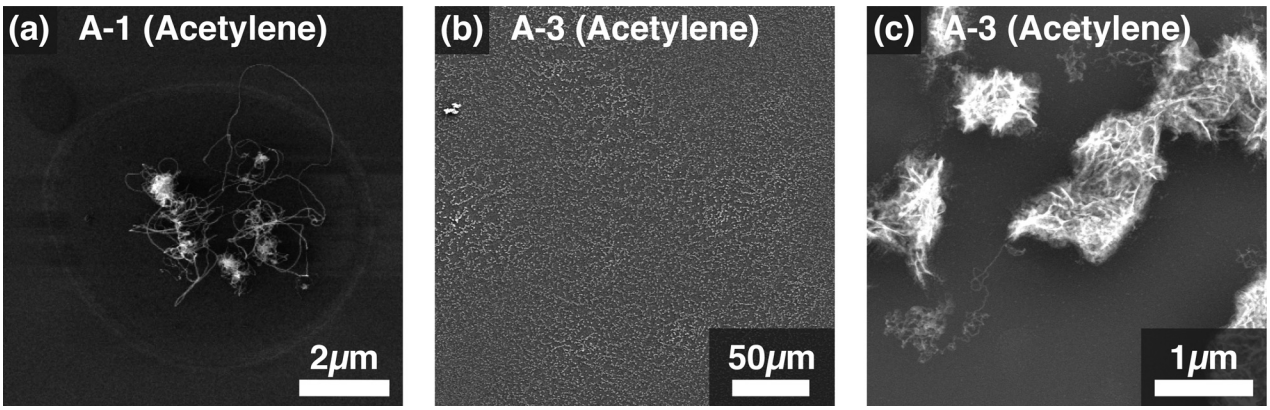

FIG. 1. Carbon nanofibrils investigated by SEM from different recipes using acetylene: (a) Representative growth morphology from recipe A-1. Carbon nanostructures of a variety of lengths and diameters are observed in crowds. (b) Representative growth morphology from recipe A-3 at low magnification. Catalyst nanoparticles are distributed evenly on the alumina substrate and carbon nanofibrils are found homogeneously. (c) A high magnification view of (b) focusing on a few agglomerates of titania nanoparticle catalysts. Micron-long fibrils extend from those catalysts.

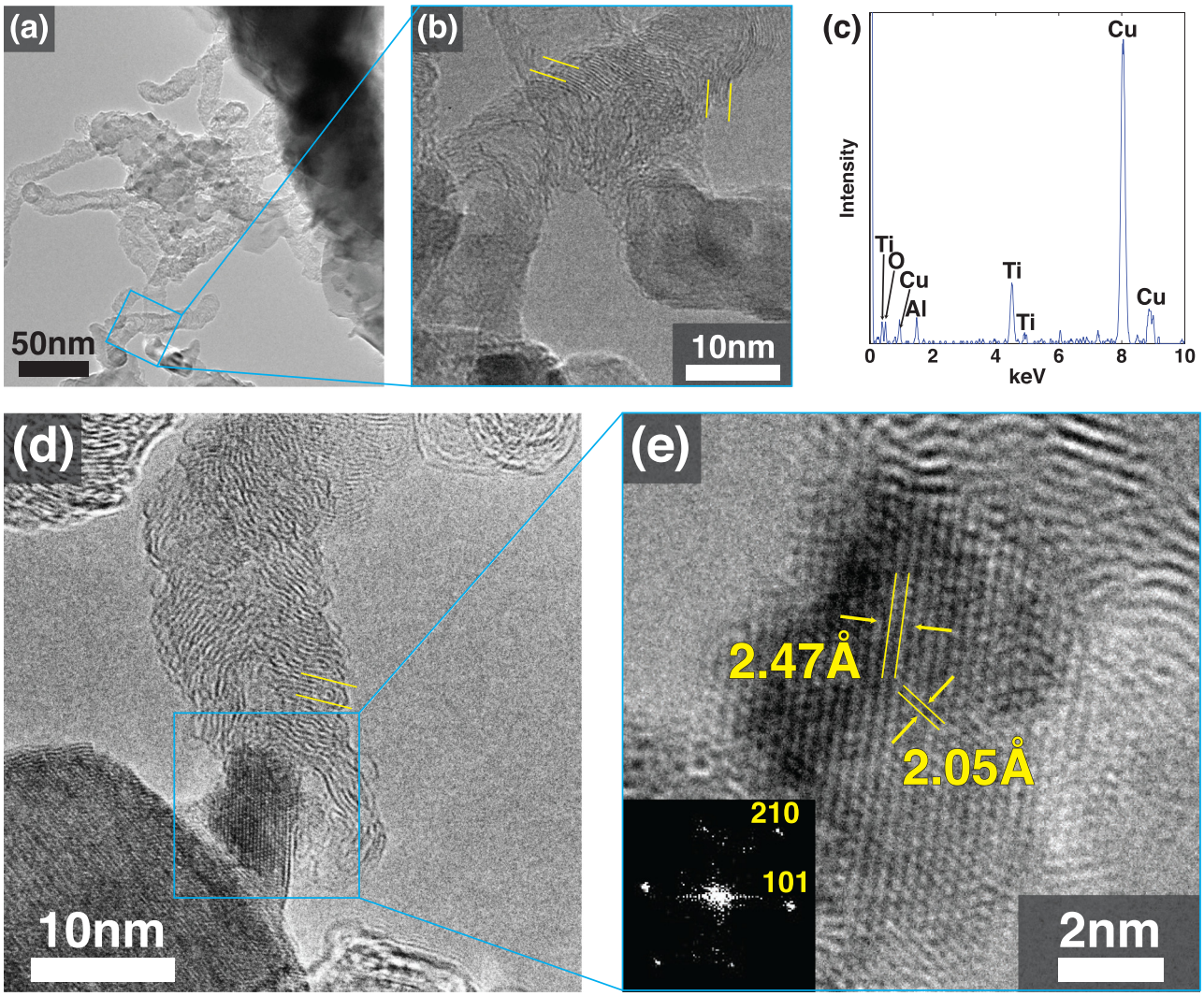

FIG. 2. Representative turbostratic CNTs from recipe A-3 growth: (a) CNTs grown from titania catalyst. Only base growth is observed, i.e., no nanoparticles observed at the tips of the CNTs. (b) Higher magnification of (a) showing the interface between a CNT and a titania nanoparticle catalyst. Few graphitic layers are found to form a bundle, indicated by yellow lines. (c) Localized EDX taken from the interface between the nanoparticle and the CNT shown in (b). Cu peaks are from the TEM grid. (d) An HRTEM image of a CNT grown from the nanoparticle catalyst. Few graphitic layers are found to form a bundle and indicated by yellow lines, similar to (b). (e) Higher magnification of (c) showing the nanoparticle catalyst with the FFT pattern. Two spots are assigned to the rutile phase titania from their corresponding lattice distances and the angle between these spots.

observations are consistent with the renowned difficulties of direct reduction from titania to titanium metal by hydrogen.[62,63] More reducing environments often employed for carbothermal synthesis of titanium carbide from titania nanoparticle precursors also agree with our observation, which include 1000 °C or higher reaction temperatures, an hour or longer reaction time, and getting titania directly in contact with a solid source of carbon.[64–68] Furthermore,

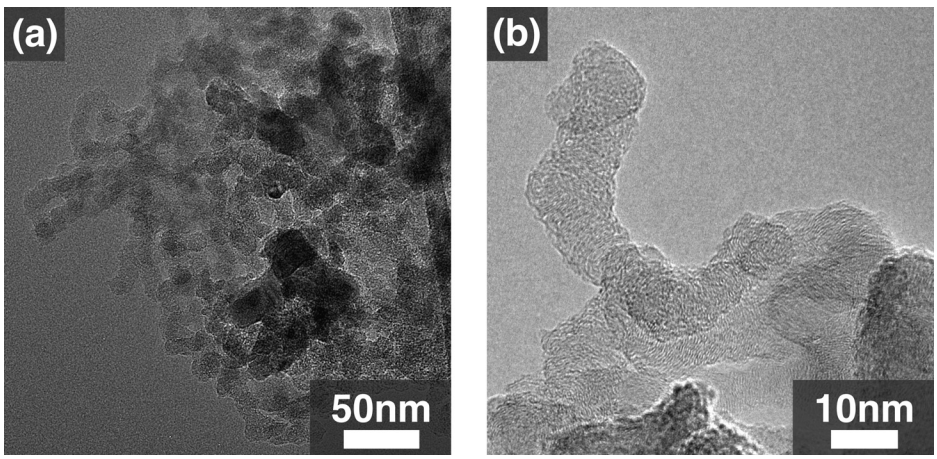

FIG. 3. Representative turbostratic CNFs from recipe A-3: (a) A dense crowd of CNFs. (b) A representative CNF grown via base growth.

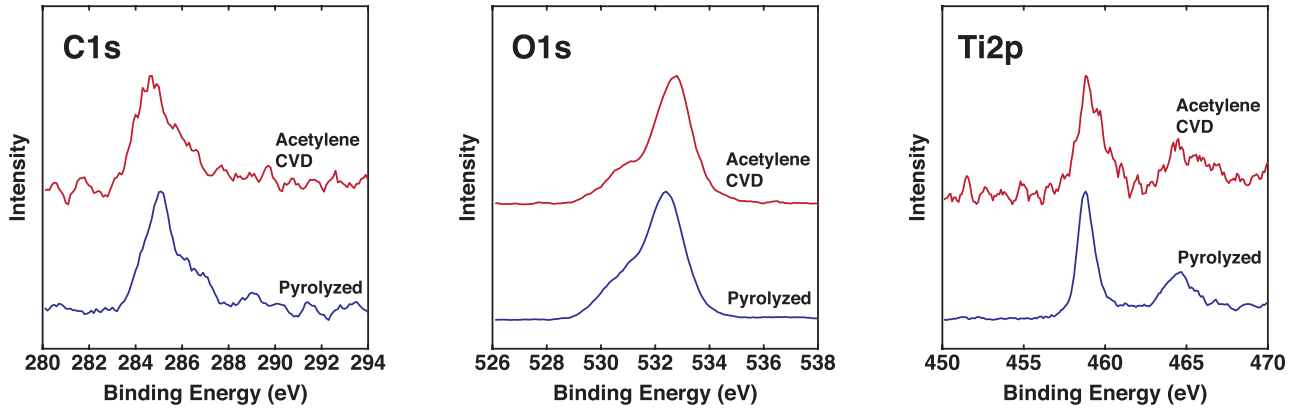

FIG. 4. XPS spectra taken from the recipe A-3 sample before and after CVD.

nanoparticles of titanium carbide are stable down to room temperature once synthesized[69] and resistant to oxidation in air up to 300 °C at atmospheric pressure.[70] Hence, the observed Ti2p peaks suggest that titania is the primary compound that contains titanium throughout the CVD growth. According to the EDX and XPS spectra, analysis on lattice fringes and the FFT pattern, and the stability of different phases of titania at our reaction temperature,[71] the nanoparticle in Fig. 2(e) is assigned to be rutile phase titania (see Table S2, supplementary material for more detail).

The HRTEM observations of CNTs and CNFs grown from titania nanoparticle catalysts and the XPS spectra from recipe A-3 growth are consistent with the Raman spectra taken at three different stages shown in Fig. 5 (as dropcast, pyrolyzed, and after CVD). The Raman spectrum after CVD implies that the titania nanoparticle catalysts convert acetylene into graphitic nanostructures after CVD, providing characteristic peaks: D peak (1339 cm^{-1}), G peak (1590 cm^{-1}), 2D peak (2669 cm^{-1}), D + D′ peak (2930 cm^{-1}), and 2D′ peak (3200 cm^{-1}).[72] The D/G peak intensity ratio indicates that the resulting graphitic structure is defect-rich,[73] while sufficient graphitization is indicated by a small contribution from amorphous carbon around 1500 cm^{-1}.[74]

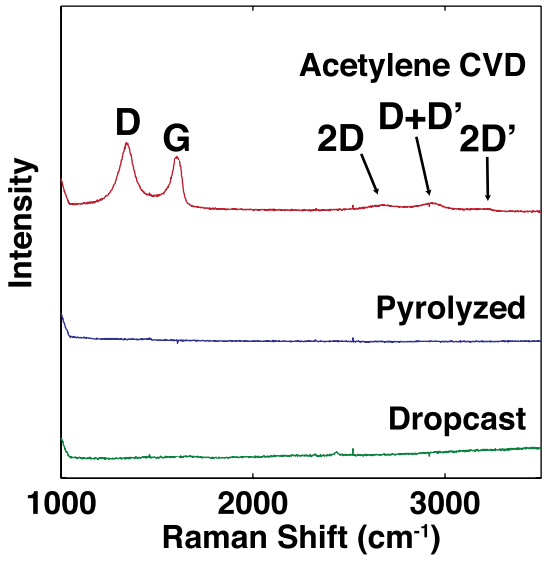

FIG. 5. Raman spectra of recipe A-3 samples after dropcasting, pyrolysis at 800 °C, and CVD at 850 °C.

Ethylene and methane carbon feedstocks were also tested. Ethylene is converted into carbon nanofibrils by titania with recipe E as shown in Fig. 6. The growth morphology shown in Fig. 6(a) resembles the result of recipe A-1 growth [Fig. 1(a)], suggesting similar growth mechanisms. For the sake of imaging the catalyst-nanofibril interface from this relatively inhomogeneous growth, CVD with recipe E is replicated on a silicon nitride TEM grid as a substrate instead of the silica substrate (details of this method are described in our previous work[21]). We found similar growth morphologies from recipe A-3, a CNT with substructures extending from a corner of the nanoparticle catalyst without graphitic cage formation [Fig. 6(b)]. The measured lattice distance most likely belongs to rutile titania as in Table S1 (supplementary material) and neither to titanium metal nor to carbide. The observed carbon nanofibrils resemble those often described as bamboo-like CNTs [Fig. 6(c)].[75]

Carbon nanofibrils are not synthesized from methane with recipe M. The reaction temperature of recipe M was set to 900 °C, since methane is more difficult to convert catalytically into CNTs than ethylene and acetylene even for metal nanoparticles such as Fe.[13] As in Fig. 7(a), no fibrils are synthesized with recipe M. However, thin graphitic layers are observed on exposed surfaces of aggregated titania nanoparticles as by TEM [Fig. 7(b)], and Raman spectroscopy corroborates that [Fig. 7(c)].

These results imply that titania nanoparticles can decompose all of the tested hydrocarbons and serve as catalysts to synthesize graphitic nanostructures. Still, the mechanisms and rates of decomposition seem comparable only between acetylene and ethylene but not methane. Acetylene, producing the highest yield, is chosen as the carbon feedstock for the basis of further discussion about growth mechanisms via titania nanoparticle catalysts.

We first discuss kinetics of CNT/CNF growth on a single catalyst nanoparticle, with acetylene as carbon feedstock. Based on the SEM and HRTEM investigations, the number of carbon atoms is estimated for the observed turbostratic CNTs and CNFs by idealizing the carbon nanofibrils as crystalline CNFs, and also for the CNTs grown as baseline with Fe catalysts (see Fig. S2, supplementary material). The baseline growth with Fe was processed with exactly the same CVD parameters as recipe A-3. Representative values for

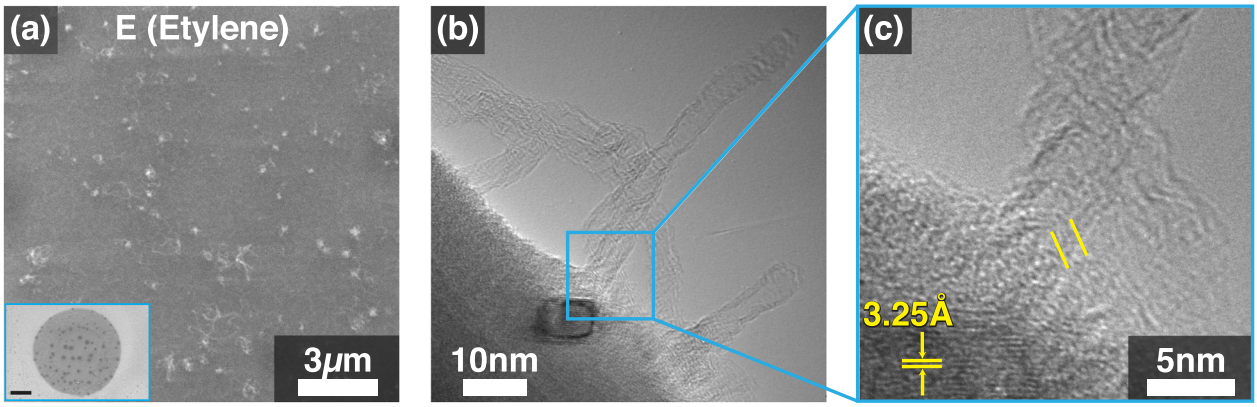

FIG. 6. Recipe E growth investigated by SEM and HRTEM. (a) Representative growth morphology by recipe E which is similar to Fig. 1(a). The inset is the low magnification view showing the receded precursor residue spot with a scale bar 20 μm. (b) A CNT extending from a titania NP catalyst observed from the recipe E sample replicated on a silicon nitride TEM grid. (c) A higher magnification of (b) focusing on the catalyst-CNT interface. A stack of graphitic layers is annotated by parallel yellow lines.

length, diameter, and the number of walls are determined by sampling and measuring from SEM and TEM micrographs. The details and results of this estimation are summarized in the supplementary material, Sec. III. In the case of microns-long CNTs/CNFs, the mean carbon assembly rate on titania nanoparticle catalysts may be comparable to iron. However, titania nanoparticle catalysts more often grow shorter CNTs/CNFs; thus, the catalytic activity per catalyst nanoparticle is lower than Fe by an order of magnitude, with the CVD parameters employed in recipe A-3. Formation of CNTs/CNFs from Fe nanoparticle catalysts involves precipitation of supersaturated carbon, which reduces the total free energy of the system according to the Fe-C phase diagram[6,76] and therefore spontaneously occurs. Since the growth morphology suggests surface-bound mechanisms, formation of CNTs/CNFs from titania nanoparticles does not necessarily reduce the total free energy in the same way and potentially decreases the catalytic activity compared to Fe. Different etching rates of carbon by hydrogen between titania and Fe catalysts may also contribute to the difference in their catalytic activities.[77,78] A more precise quantitative comparison based on the number density of growth, instead of single catalyst-based estimation, requires time-evolution of the assembly rate.[79]

Next, we propose a lift-off mechanism of graphitic layers based on simple multilayer graphene structural energetics at the nanoparticle corner. The nanoparticle corner is a more active site for adsorption and reaction than a flat surface due to higher surface defect density.[80] Therefore, accumulated acetylene molecules are decomposed into a cluster of carbon atoms and eventually transformed to graphene layers, while on other portions of the surface they tend to detach by hydrogenation,[81,82] leaving the surface before decomposition. We start with one or more layers of graphene grown over a 2D corner of a nanoparticle catalyst where two facets meet at the angle α (see Fig. 8), as the most basic representation of geometries observed by HRTEM. The multilayer graphene is bent at a curvature of radius R, storing bending strain energy that increases with the number of graphitic layers. As the multilayer graphene grows thicker, it will eventually lift off in order to relax this strain. Here we adopt a formulation by Zhang *et al.* regarding the relationship between bending strain energy E, the number of graphitic layers n, the catalyst angle α, and the second

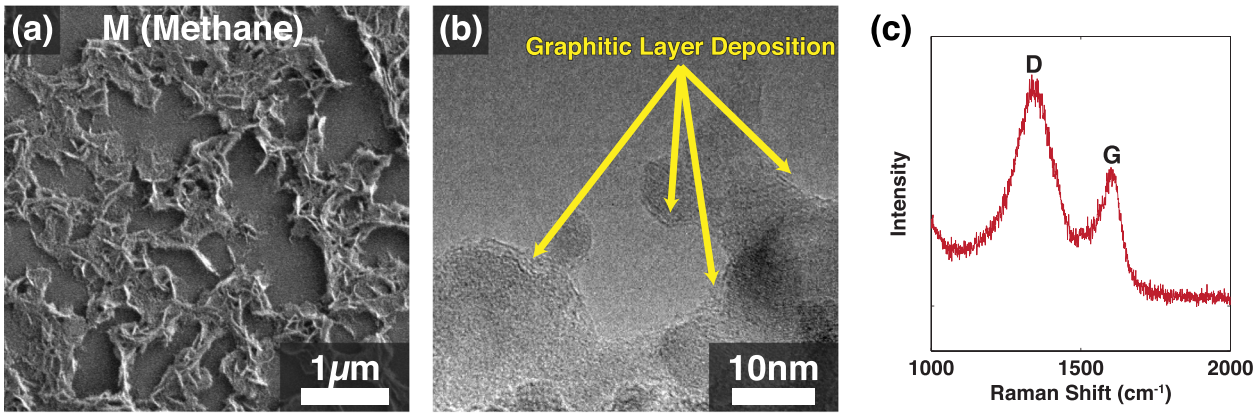

FIG. 7. Recipe M samples investigated by SEM, HRTEM, and Raman spectroscopy showing nor growth of carbon nanofibrils. (a) SEM image of uniformly deposited titania catalyst with no growth of CNTs/CNFs observed. (b) HRTEM image of titania nanoparticles. A thin graphitic layer covers the exposed surface of the aggregated nanoparticles continuously. (c) A Raman spectrum of (a). Defect-rich graphite is indicated by the high D/G ratio.

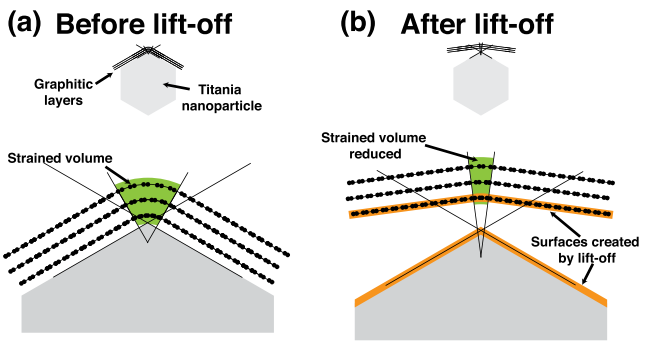

FIG. 8. Schematic illustrations showing graphitic layer lift-off based on the plate model for the multilayer graphene ($n = 3$). (a) Before lift-off. The green area indicates the portion of the multilayer graphene where strain energy is stored. (b) After lift-off. Bending strain is relaxed and new surfaces are created as indicated by orange arrows. The z-axis is perpendicular to the figures.

derivative of the bending energy density "Eb" as $\kappa_{(n)}$.[83] Zhang *et al*. deal with the multilayer graphene by assuming perfect bonding between the layers as in the classic treatment of a solid (or layered) plate in bending following the Kirchhoff hypothesis for bending,[84] and our "plate model" adopts their method. Due to the potential for inter-layer compliance (i.e., imperfect layer bonding), we also calculate the limiting case of non-interacting layers as well and label that the "individual layer model." For the "plate model" and the "individual layer model," we calculate the total strain energy as function of n and α, $E_{plate(n,\alpha)}$ and $E_{indiv(n,\alpha)}$, respectively (see Figs. S3 and S4, supplementary material). The layers in the multilayer graphene interact with each other primarily via Van der Waals force, since sp^3 and amorphous carbon may present only in a minor amount compared to sp^2 carbon as observed by Raman spectroscopy (see Fig. 5). Therefore, the behavior is bounded by these two cases. The bent multilayer graphene is formed over the catalyst corner surface, and the distance between the titania catalyst surface and the multilayer graphene d is estimated from the thickness of single layer graphene on insulator substrates measured by atomic force microscope (AFM)[85,86] and the Van der Waals diameter of a carbon atom.[87] Details of how the bending strain energy for the plate model $E_{plate(n,\alpha)}$ and the individual layer model $E_{indiv(n,\alpha)}$ were calculated are available in the supplementary material, Sec. IV.

When lift-off occurs with an interfacial area A, the bending strain energy is at least as high as the sum of the surface energy associated with creating surfaces of both the graphitic layer and the titania nanoparticle [see Fig. 8(b)]. In terms of thermodynamics, we can formulate the condition for lift off as follows:[88]

$$E_{(n,\alpha)} + \gamma_1 A \geq E_{(n,\beta)} + (\gamma_2 + \gamma_3)A, \tag{1}$$

where γ_1 is the interfacial energy between the graphitic layer and the nanoparticle catalyst, γ_2 is the surface energy of graphitic layer, and γ_3 is the surface energy of nanoparticle catalyst. By introducing adhesion energy of multilayer graphene on the nanoparticle catalyst Γ, we derive the condition for lift-off as follows:

$$E_{(n,\alpha)} \geq E_{(n,\beta)} + \Gamma A. \tag{2}$$

The adhesion energy of graphene varies with both the number of layers and the substrate that graphene grows on.[89–91] Although the adhesion energy between graphene and metal oxides has not been previously reported, the value can be estimated by assuming that graphene on silica is more similar to our situation than graphene on metals. The interaction between graphene and the underlying substrates is due to Van der Waals interaction,[92] and hence magnitude of the interaction depends on the surface electron density of the substrate material. Therefore, in this work, we use the adhesion energy experimentally measured by He *et al*. on silica.[90] They reported that the adhesion energy of graphene on silica decreases rapidly as the number of layers increases: 0.47 J/m^2 for a single layer graphene, 0.35 J/m^2 for a bilayer graphene, and ~0.3 J/m^2 for a trilayer or thicker graphene,[90] which is comparable to the values measured by Koenig *et al*.[91] In our case, the interfacial area between the graphitic layer and the corner of the nanoparticle is approximately 100 nm^2, given ~10 nm of the diameter of the nanoparticle catalysts. Therefore, the threshold energy for $E_{plate(n,\alpha)}$ and $E_{indiv(n,\alpha)}$ required for lift-off is 293 eV for a single layer graphene, 218 eV for a bilayer graphene, and ~187 eV for a trilayer or thicker graphene.

$E_{plate(n,\alpha)}$ and $E_{indiv(n,\alpha)}$ as functions of the number of graphitic layers n for selected catalyst angles α are plotted in Fig. 9. Figure 9(a) shows that $E_{plate(n,\alpha)}$ rapidly increases especially for α steeper than 130°. For a given α, if greater than two layers, the plate model predicts that the strain energy can become more than 5 times higher than the threshold energy (indicated by red stars in Fig. 9). The individual layer model naturally yields a lower strain energy than the plate model as plotted in Fig. 9(b).

Bent graphitic layers, indeed, can relax the bending strain energy by forming Stone-Wales defects,[93] as some of CNTs and CNFs investigated in this work have graphitic layers that are still bent after lift-off. The shear modulus of turbostratic graphite C_{44} is about one-tenth of that of pristine graphite;[94,95] thus, inter-layer compliance is not negligible. More complicated geometry than the 2D estimation used here also potentially occurs, such as a corner of a polyhedron where three or more facets meet and/or multiple corners located close enough where graphitic layers are bent more than once. Still, according to the model, combined with HRTEM investigation in this work, strain energy stored in the bent graphitic layers formed over a catalyst corner can be one of the major driving forces for lift-off. It is worthwhile to note that the lack of CNT/CNF growth from recipe M which uses methane is also explained by the presented model. According to the model presented, a thin graphitic layer with large interfacial area as observed in Fig. 7(b) resists lift-off and thus does not initiate CNT/CNF growth. This model may also partially explain that CNTs and CNFs grow on geometries such as roughened surface or nanoporous structures, without using metal nanoparticle catalysts.[96] As a summary, Fig. 10 schematically illustrates how repetitive lift-off of graphitic layers bent over a nanoparticle corner in a 2D mode leads to carbon nanofibrils we observe

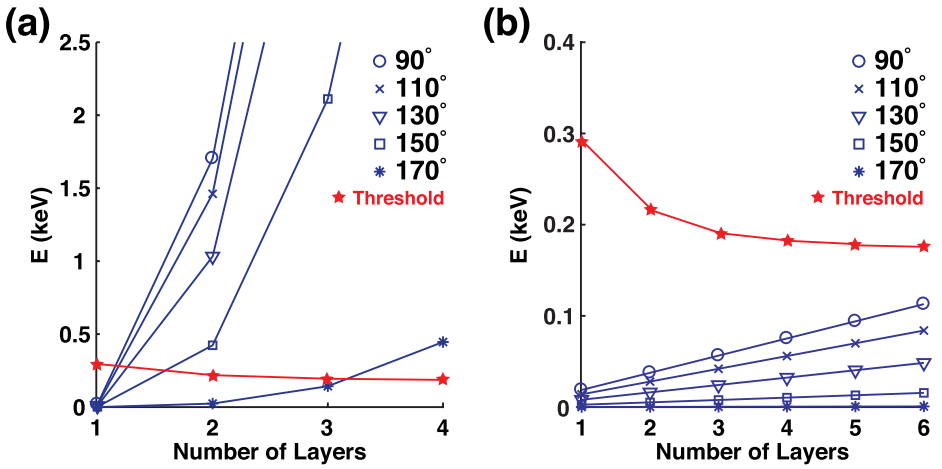

FIG. 9. Energy balance for lift-off with selected catalyst angles α calculated with the proposed model. (a) Results from the plate model. (b) Results from the individual layer model. Calculations of energies are for the estimated interfacial area, approximately 100 nm^2, between the graphitic layer and the corner of the nanoparticle, following from observed diameters of nanoparticle catalysts of ~10 nm. Approximate threshold energies of lift-off for each number of graphitic layers are indicated by the red stars.

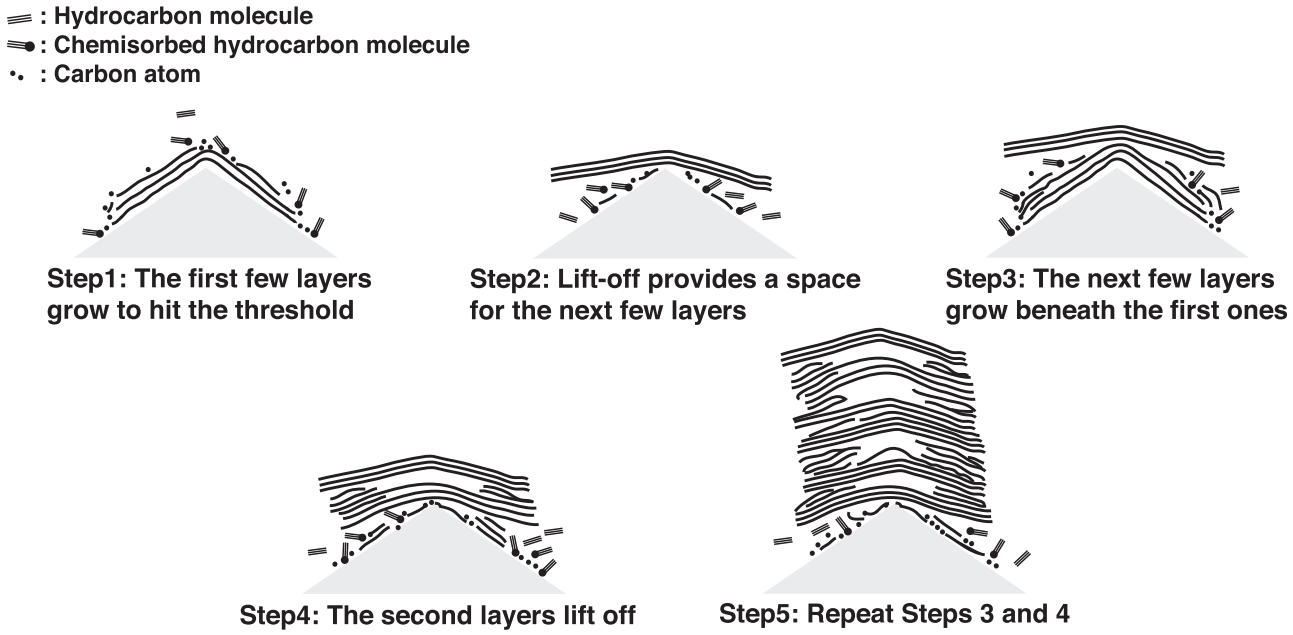

FIG. 10. Schematic illustration of growth model based on the repetitive lift-off of strained multilayer graphene stacks.

with titania nanoparticles. If the bending strain energy is partially dissipated as mentioned above, each substructure needs more graphitic layers for lift-off and the bending strain may not be fully released, resulting in turbostratic CNTs (Fig. 2). If lift-off occurs at small number of graphitic layers and every substructure intimately contacts with the substructure previously lift off, the resulting nanofibril will likely be turbostratic CNFs (Fig. 3).

IV. CONCLUSIONS

Using acetylene and ethylene as carbon feedstock and titania nanoparticles as catalysts, we synthesize turbostratic CNTs and CNFs. The highest growth yield and homogeneity on the substrate are obtained employing acetylene, alumina substrate, and reaction at 850 °C. The estimation on the number of acetylene molecules converted into CNT/CNFs on a single titania nanoparticle catalyst indicates about an order of magnitude lower catalytic activity for titania compared with Fe. This may be attributed to the difference in the growth mechanisms: solution-precipitation or surface-bound process. Further, in-detail studies on growth kinetics such as *in-situ* investigations will be a future work. A quantitative lift-off model for graphitic layers formed over a 2D corner of a titania catalyst nanoparticle is provided. The model is based on the balance between bending strain energy and interfacial energy before and after the lift-off, and the angle of the corner plays a role in conditions to determine lift-off of the graphitic layers. This model explains a key differentiating feature of turbostratic CNT/CNF growth via non-metallic nanoparticles.

SUPPLEMENTARY MATERIAL

See supplementary material for control samples, crystallographic data to exclude metal contamination, estimation of carbon assembly rates, and the details of energy balance calculation.

ACKNOWLEDGMENTS

This material is based upon work supported by the National Science Foundation under Grant No. 1007793 and was also supported by Airbus, Boeing, Embraer, Lockheed Martin, Saab AB, Spirit AeroSystems Inc., Textron Systems, ANSYS, Hexcel, and TohoTenax through MIT's Nano-Engineered Composite aerospace STructures (NECST) Consortium. This research was supported (in part) by the U.S. Army Research Office under Contract No. W911NF-13-D-0001. This work was performed in part at the Center for Nanoscale Systems (CNS), a member of the National Nanotechnology Infrastructure Network (NNIN), which is supported by the National Science Foundation under NSF Award No. ECS-0335765. CNS is part of Harvard University. This work was carried out in part through the use of MIT Microsystems Technology Laboratories. Stephan Hofmann acknowledges funding from EPSRC under Grant No. EP/H047565/1. Akira Kudo acknowledges Itai Y. Stein (MIT) for helpful discussion.

[1]Y. L. Li, I. A. Kinloch, and A. H. Windle, Science **304**, 276 (2004).
[2]X. Li, X. Wang, L. Zhang, S. Lee, and H. Dai, Science **319**, 1229 (2008).
[3]M. M. Shulaker, G. Hills, N. Patil, H. Wei, H. Y. Chen, H. S. P. Wong, and S. Mitra, Nature **501**, 526 (2013).
[4]X. Wang, L. Zhi, and K. Mullen, Nano Lett. **8**, 323 (2008).
[5]A. L. M. Reddy, M. M. Shaijumon, S. R. Gowda, and P. M. Ajayan, Nano Lett. **9**, 1002 (2009).
[6]C. T. Wirth, B. C. Bayer, A. D. Gamalski, S. Esconjauregui, R. S. Weatherup, C. Ducati, C. Baehtz, J. Robertson, and S. Hofmann, Chem. Mater. **24**, 4633 (2012).
[7]B. C. Bayer, C. Baehtz, P. R. Kidambi, R. S. Weatherup, C. Mangler, J. Kotakoski, C. J. L. Goddard, S. Caneva, A. Cabrero-Vilatela, J. C. Meyer, and S. Hofmann, Appl. Phys. Lett. **105**, 143111 (2014).
[8]S. Esconjauregui, C. M. Whelan, and K. Maex, Carbon **47**, 659 (2009).
[9]S. A. Steiner III, R. Li, and B. L. Wardle, ACS Appl. Mater. Interfaces **5**, 4892 (2013).
[10]C. Ge, Y. Li, J. J. Yin, Y. Liu, L. Wang, Y. Zhao, and C. Chen, NPG Asia Mater. **4**, e32 (2012).
[11]S. Steiner III, T. Baumann, B. Bayer, R. Blume, M. Worsley, W. MoberlyChan, E. Shaw, R. Schlogl, A. Hart, S. Hofmann, and B. Wardle, J. Am. Chem. Soc. **131**, 12144 (2009).
[12]L. Zhang, C. Liu, B. Liu, W. Yu, P. Hou, and H. Cheng, Carbon **55**, 253 (2013).
[13]B. C. Bayer, C. Castellarin-Cudia, R. Blume, S. A. Steiner, C. Ducati, D. Chu, A. Goldoni, A. Knop-Gericke, R. Schlögl, C. Cepek, J. Robertson, and S. Hofmann, RSC Adv. **3**, 4086 (2013).
[14]H. Liu, D. Takagi, H. Ohno, S. Chiashi, T. Chokan, and Y. Homma, Appl. Phys. Express **1**, 014001 (2008).
[15]A. Bachmatiuk, R. G. Mendes, C. Hirsch, C. Jähne, M. R. Lohe, J. Grothe, S. Kaskel, L. Fu, R. Klingeler, J. Eckert, P. Wick, and M. H. Rümmeli, ACS Nano **7**, 10552 (2013).
[16]M. Rümmeli, A. Bachmatiuk, A. Scott, F. Börrnert, J. Warner, V. Hoffman, J. Lin, G. Cuniberti, and B. Büchner, ACS Nano **4**, 4206 (2010).
[17]P. R. Kidambi, B. C. Bayer, R. S. Weatherup, R. Ochs, C. Ducati, D. V. Szabó, and S. Hofmann, Phys. Status Solidi RRL **5**, 341 (2011).
[18]D. Takagi, H. Hibino, S. Suzuki, Y. Kobayashi, and Y. Homma, Nano Lett. **7**, 2272 (2007).
[19]B. Liu, W. Ren, L. Gao, S. Li, S. Pei, C. Liu, C. Jiang, and H. Cheng, J. Am. Chem. Soc. **131**, 2082 (2009).
[20]D. Takagi, Y. Kobayashi, and Y. Homma, J. Am. Chem. Soc. **131**, 6922 (2009).
[21]A. Kudo, S. A. Steiner III, B. C. Bayer, P. R. Kidambi, S. Hofmann, M. S. Strano, and B. L. Wardle, J. Am. Chem. Soc. **136**, 17808 (2014).
[22]L. L. Tan, W. J. Ong, S. P. Chai, and A. R. Mohamed, Catal. Today **217**, 1 (2013).
[23]Y. Homma, H. Liu, D. Takagi, and Y. Kobayashi, Nano Res. **2**, 793 (2009).
[24]B. Liu, W. Ren, C. Liu, C. Sun, L. Gao, S. Li, C. Jiang, and H. Cheng, ACS Nano **3**, 3421 (2009).
[25]T. Y. Liu, L. L. Zhang, W. J. Yu, S. S. Li, P. X. Hou, H. T. Cong, C. Liu, and H. M. Cheng, Carbon **56**, 167 (2013).
[26]S. Huang, Q. Cai, J. Chen, Y. Qian, and L. Zhang, J. Am. Chem. Soc. **131**, 2094 (2009).
[27]L. Kang, Y. Hu, L. Liu, J. Wu, S. Zhang, Q. Zhao, F. Ding, Q. Li, and J. Zhang, Nano Lett. **15**, 403 (2015).
[28]Q. Cai, Y. Hu, Y. Liu, and S. Huang, Appl. Surf. Sci. **258**, 8019 (2012).
[29]Y. Chen and J. Zhang, Carbon **49**, 3316 (2011).
[30]H. Liu, D. Takagi, S. Chiashi, and Y. Homma, Carbon **48**, 114 (2010).
[31]A. Bachmatiuk, F. Börrnert, V. Hoffmann, D. Lindackers, J.-H. Lin, B. Büchner, and M. H. Rümmeli, J. Appl. Phys. **109**, 094317 (2011).
[32]J. Kong, A. M. Cassell, and H. Dai, Chem. Phys. Lett. **292**, 567 (1998).
[33]S. Maruyama, R. Kojima, Y. Miyauchi, S. Chiashi, and M. Kohno, Chem. Phys. Lett. **360**, 229 (2002).
[34]K. Mukhopadhyay, A. Koshio, T. Sugai, N. Tanaka, H. Shinohara, Z. Konya, and J. B. Nagy, Chem. Phys. Lett. **303**, 117 (1999).
[35]D. Takagi, Y. Homma, H. Hibino, S. Suzuki, and Y. Kobayashi, Nano Lett. **6**, 2642 (2006).
[36]S. Hofmann, R. Sharma, C. Ducati, G. Du, C. Mattevi, C. Cepek, M. Cantoro, S. Pisana, A. Parvez, F. Cervantes-Sodi, A. C. Ferrari, R. Dunin-Borkowski, S. Lizzit, L. Petaccia, A. Goldoni, and J. Robertson, Nano Lett. **7**, 602 (2007).
[37]F. Ding, P. Larsson, J. A. Larsson, R. Ahuja, H. Duan, A. Rosen, and K. Bolton, Nano Lett. **8**, 463 (2008).
[38]B. C. Bayer, S. Hofmann, C. Castellarin-Cudia, R. Blume, C. Baehtz, S. Esconjauregui, C. T. Wirth, R. A. Oliver, C. Ducati, A. Knop-Gericke, R. Schlögl, A. Goldoni, C. Cepek, and J. Robertson, J. Phys. Chem. C **115**, 4359 (2011).
[39]R. Cartwright, S. Esconjauregui, D. Hardeman, S. Bhardwaj, R. Weatherup, Y. Guo, L. D'Arsié, B. Bayer, P. Kidambi, S. Hofmann, E. Wright, J. Clarke, D. Oakes, C. Cepek, and J. Robertson, Carbon **81**, 639 (2015).
[40]A. A. Puretzky, D. B. Geohegan, S. Jesse, I. N. Ivanov, and G. Eres, Appl. Phys. A **81**, 223 (2005).
[41]J. Robertson, J. Mater. Chem. **22**, 19858 (2012).
[42]M. H. Rümmeli, F. Schäffel, A. Bachmatiuk, D. Adebimpe, G. Trotter, F. Börrnert, A. Scott, E. Coric, M. Sparing, B. Rellinghaus, P. G. McCormick, G. Cuniberti, M. Knupfer, L. Schultz, and B. Büchner, ACS Nano **4**, 1146 (2010).
[43]M. H. Rümmeli, F. Schäffel, C. Kramberger, T. Gemming, A. Bachmatiuk, R. J. Kalenczuk, B. Rellinghaus, B. Büchner, and T. Pichler, J. Am. Chem. Soc. **129**, 15772 (2007).
[44]P. Pietrokowsky, J. Appl. Phys. **37**, 4560 (1966).
[45]Z. S. Basinski, W. Hume-Rothery, and A. L. Sutton, Proc. R. Soc. London, Ser. A: Math., Phys. Eng. Sci. **229**, 459 (1955).
[46]W. C. Chiou, Jr. and E. A. Carter, Surf. Sci. **530**, 88 (2003).
[47]M. E. Straumanis and C. C. Weng, Acta Crystallogr. **8**, 367 (1955).
[48]Y. K. Vohra and P. T. Spencer, Phys. Rev. Lett. **86**, 3068 (2001).
[49]O. Senkov, B. Chakoumakos, J. Jonas, and F. Froes, Mater. Res. Bull. **36**, 1431 (2001).
[50]U. Diebold, Surf. Sci. Rep. **48**, 53 (2003).
[51]M. Guemmaz, G. Moraitis, A. Mosser, M. Khan, and J. Parlebas, J. Electron Spectrosc. Relat. Phenom. **83**, 173 (1997).
[52]R. Blyth, H. Buqa, F. Netzer, M. Ramsey, J. Besenhard, P. Golob, and M. Winter, Appl. Surf. Sci. **167**, 99 (2000).
[53]J. Yu, G. Dai, Q. Xiang, and M. Jaroniec, J. Mater. Chem. **21**, 1049 (2011).
[54]P. M. Rao, A. Wolfson, S. Kababya, S. Vega, and M. Landau, J. Catal. **232**, 210 (2005).
[55]J. Yu, J. C. Yu, W. Ho, and Z. Jiang, New J. Chem. **26**, 607 (2002).
[56]L. M. Berger, W. Gruner, E. Langholf, and S. Stolle, Int. J. Refract. Met. Hard Mater. **17**, 235 (1999).
[57]L. M. Berger, P. Ettmayer, and B. Schultrich, Int. J. Refract. Met. Hard Mater. **12**, 161 (1993).
[58]J. Y. Shin, J. H. Joo, D. Samuelis, and J. Maier, Chem. Mater. **24**, 543 (2012).
[59]J. Qiu, S. Li, E. Gray, H. Liu, Q.-F. Gu, C. Sun, C. Lai, H. Zhao, and S. Zhang, J. Phys. Chem. C **118**, 8824 (2014).
[60]M. M. Ottakam Thotiyl, S. A. Freunberger, Z. Peng, Y. Chen, Z. Liu, and P. G. Bruce, Nat. Mater. **12**, 1050 (2013).
[61]I. Milosev, M. Metikos-Hukovic, and H. H. Strehblow, Biomaterials **21**, 2103 (2000).

[62]K. C. Sabat, P. Rajput, R. K. Paramguru, B. Bhoi, and B. K. Mishra, Plasma Chem. Plasma Process. **34**, 1 (2014).
[63]T. Kitamura, K. Shibata, and K. Takeda, ISIJ Int. **33**, 1150 (1993).
[64]H. P. Gou, G. H. Zhang, and K. C. Chou, J. Mater. Sci. **51**, 7008 (2016).
[65]Y. Gotoh, K. Fujimura, M. Koike, Y. Ohkoshi, M. Nagura, K. Akamatsu, and S. Deki, Mater. Res. Bull. **36**, 2263 (2001).
[66]S. T. Bae, H. Shin, H. S. Jung, and K. S. Hong, J. Am. Ceram. Soc. **92**, 2512 (2009).
[67]X. Li, L. Liu, S. Ge, S. Shen, J. Song, Y. Zhang, and P. Li, Carbon **39**, 827 (2001).
[68]R. Koc and J. S. Folmer, J. Am. Ceram. Soc. **80**, 952 (1997).
[69]Z. Cao, W. Xie, I. H. Jung, G. Du, and Z. Qiao, Metall. Mater. Trans. B **46**, 1782 (2015).
[70]M. Gherrab, V. Garnier, S. Gavarini, N. Millard-Pinard, and S. Cardinal, Int. J. Refract. Met. Hard Mater. **41**, 590 (2013).
[71]H. Zhang and J. F. Banfield, J. Phys. Chem. B **104**, 3481 (2000).
[72]A. C. Ferrari and D. M. Basko, Nat. Nanotechnol. **8**, 235 (2013).
[73]B. Rebollo-Plata, R. Lozada-Morales, R. Palomino-Merino, O. Portillo-Moreno, S. Jiménez-Sandoval, and O. Zelaya-Angel, in XIV International Materials Research Congress Symposium [Mater. Charact. **58**, 809 (2007)].
[74]P. K. Chu and L. Li, Mater. Chem. Phys. **96**, 253 (2006).
[75]M. Lin, J. P. Y. Tan, C. Boothroyd, K. P. Loh, E. S. Tok, and Y. L. Foo, Nano Lett. **7**, 2234 (2007).
[76]M. Singleton and P. Nash, Bull. Alloy Phase Diagrams **10**, 121 (1989).
[77]I. Vlassiouk, M. Regmi, P. Fulvio, S. Dai, P. Datskos, G. Eres, and S. Smirnov, ACS Nano **5**, 6069 (2011).
[78]E. Vietzke, K. Flaskamp, V. Philipps, G. Esser, P. Wienhold, and J. Winter, J. Nucl. Mater. **145–147**, 443 (1987).
[79]M. Bedewy, E. R. Meshot, H. Guo, E. A. Verploegen, W. Lu, and A. J. Hart, J. Phys. Chem. C **113**, 20576 (2009).
[80]M. Batzill, Energy Environ. Sci. **4**, 3275 (2011).
[81]H. P. Koh and R. Hughes, J. Catal. **33**, 7 (1974).
[82]A. C. Gluhoi, J. W. Bakker, and B. E. Nieuwenhuys, Catal. Today **154**, 13 (2010).
[83]D. B. Zhang, E. Akatyeva, and T. Dumitrică, Phys. Rev. Lett. **106**, 255503 (2011).
[84]S. Timoshenko and S. Woinowsky-Krieger, *Theory of Plates and Shells* (McGraw-Hill Publications, 1959).
[85]M. Ishigami, J. H. Chen, W. G. Cullen, M. S. Fuhrer, and E. D. Williams, Nano Lett. **7**, 1643 (2007).
[86]T. Tsukamoto and T. Ogino, Appl. Phys. Express **2**, 075502 (2009).
[87]S. C. O'Hern, D. Jang, S. Bose, J.-C. Idrobo, Y. Song, T. Laoui, J. Kong, and R. Karnik, Nano Lett. **15**, 3254 (2015).
[88]H. B. Callen, *Thermodynamics and an Introduction to Thermostatistics* (John Wiley & Sons, 1985).
[89]T. Yoon, W. C. Shin, T. Y. Kim, J. H. Mun, T. S. Kim, and B. J. Cho, Nano Lett. **12**, 1448 (2012).
[90]Y. He, W. F. Chen, W. B. Yu, G. Ouyang, and G. W. Yang, Sci. Rep. **3**, 2660 (2013).
[91]S. P. Koenig, N. G. Boddeti, M. L. Dunn, and J. S. Bunch, Nat. Nanotechnol. **6**, 543 (2011).
[92]Z. H. Aitken and R. Huang, J. Appl. Phys. **107**, 123531 (2010).
[93]E. Ertekin, D. C. Chrzan, and M. S. Daw, Phys. Rev. B **79**, 155421 (2009).
[94]O. L. Blakslee, D. G. Proctor, E. J. Seldin, G. B. Spence, and T. Weng, J. Appl. Phys. **41**, 3373 (1970).
[95]A. Bosak, M. Krisch, M. Mohr, J. Maultzsch, and C. Thomsen, Phys. Rev. B **75**, 153408 (2007).
[96]E. Bae, W. Choi, K. Jeong, J. Chu, G.-S. Park, S. Song, and I. Yoo, Adv. Mater. **14**, 277 (2002).